Results in Engineering 28 (2025) 107376

Contents lists available at ScienceDirect

Results in Engineering

journal homepage: www.sciencedirect.com/journal/results-in-engineering

Research paper

Optical fiber integration in PDMS devices for dynamic tissue deformation

Antonio Velarte [a,*], Andrea Sannino [b], Aranzazu Otin [b], Beatriz Santamaría [c,d,e], José Ignacio Artigas [b], Esther Pueyo [a,f]

[a] Biomedical Signal Interpretation and Computational Simulation (BSICoS) Group, I3A Institute, IIS Aragón, University of Zaragoza, Zaragoza, 50018, Spain
[b] Power Electronics and Microelectronics (GEPM) Group, I3A Institute, University of Zaragoza, Zaragoza, 50018, Spain
[c] Group of Optics, Photonics, and Biophotonics, Center for Biomedical Technology (CTB), Universidad Politécnica de Madrid, Parque Científico y Tecnológico de la UPM, Campus de Montegancedo, M-40, km 38, 28223 Pozuelo de Alarcón, Madrid, Spain
[d] Group of Organ and Tissue on-a-chip and In-Vitro Detection, Health Research Institute of the Hospital Clínico San Carlos, IdISSC, C/ Profesor Martín Lagos s/n, 4ª Planta Sur 28040, Madrid, Spain
[e] Department of Mechanics, Chemistry and Industrial Design Engineering, Escuela Superior de Ingeniería y Diseño Industrial, Universidad Politécnica de Madrid, Ronda de Valencia 3, 28012, Madrid, Spain
[f] Centro de Investigación Biomédica en Red (CIBER) de Bioingeniería, Biomateriales y Nanomedicina (CIBER-BBN), Madrid, 28029, Spain

ARTICLE INFO

Keywords:
PDMS membrane
Optical fiber sensing
Stretch sensing
Tissue engineering
Biomechanical actuation

ABSTRACT

This study introduces an advanced optical fiber-based stretchable sensing platform designed for precise biomechanical characterization in tissue engineering applications, specifically tailored for cardiac tissue studies. The system is entirely fabricated from biocompatible polydimethylsiloxane (PDMS) material, and features a thin upper membrane and an internal cavity where controlled pneumatic deformation occurs. Deformation is quantified through changes in optical intensity measured through a strategically aligned optical fiber pair, as membrane stretching disrupts total internal reflection conditions. Finite element modeling using COMSOL is used to optimize device geometry and predict deformation, which is subsequently validated through experimental analyses. A custom-designed electronic system with capacity for real-time signal processing ensures stable and sensitive data acquisition. The experimental results show high levels of linearity and repeatability in a physiologically relevant stretch range, highlighting its potential for biomechanical research applications and dynamic tissue stimulation. Future improvements are directed toward extending the reliable deformation operating range through advances in the optical system.

1. Introduction

Cardiovascular diseases (CVDs) are the leading cause of global mortality. They are responsible for more than 18 million deaths annually and projections indicate a 73.4% increase in mortality figures by 2050, significantly affecting the capacity of healthcare systems [1–3]. Despite advances in prevention and treatment, a critical barrier to progress lies in the limitations of current preclinical models, which often fail to replicate the mechanical and functional complexities of the human heart. Advanced methodologies that integrate precise measurements of electrical and mechanical properties of cardiac tissues are urgently needed to bridge the gap between basic research and clinical applications [4,5].

In recent decades, cardiac tissue slices have emerged and have been validated as a physiologically relevant model in cardiovascular research [6–8]. Unlike traditional *in vitro* models, which often oversimplify the biomechanical dynamics of the heart, cardiac slices preserve key aspects of native tissue, such as its structure and functionality [9]. These features make them highly suitable for studying contractility, electrophysiology, and tissue mechanics under controlled conditions. In addition, tissue slices provide a reliable model for investigating the impact of mechanical stress on cardiac function, which is key to understanding how such stress affects cardiac performance and pathology.

The accurate application and measurement of tissue deformation is particularly relevant in the evaluation of biomechanical tissue properties in fields such as tissue engineering and regenerative medicine and in the development of therapeutic interventions. Over the years, various techniques have been developed to quantify deformation, such as strain gauges, piezoelectric sensors [10], and magnetic field-based

* Corresponding author.
E-mail addresses: avelarte@unizar.es (A. Velarte), asannino@unizar.es (A. Sannino), aranotin@unizar.es (A. Otin), beatriz.santamaria@ctb.upm.es (B. Santamaría), jiartigas@unizar.es (J.I. Artigas), epueyo@unizar.es (E. Pueyo).

https://doi.org/10.1016/j.rineng.2025.107376
Received 18 June 2025; Received in revised form 1 September 2025; Accepted 18 September 2025

Available online 22 September 2025

systems [11], each offering distinct advantages and limitations. Similarly, techniques have been proposed to apply static mechanical loads [12,13] or controlled deformation patterns, such as motorized actuators [14], force-controlled platforms [15], and air-pressure-driven systems [16]. Integrated platforms, such as Cytostretch [17] and MyoLoop [18], further advance these capabilities by combining mechanical deformation and measurement in a single system, thus providing novel tools for mechanobiological studies. The choice of a suitable technique to measure or apply tissue deformation is crucial, as it directly affects the precision, sensitivity, and reliability of the experimental results.

Among recent strategies for mechanical stimulation, pneumatic systems provide a versatile and practical alternative to apply deformation to soft biological tissues. By modulating air pressure, they generate smooth and uniform stretch patterns that replicate physiological loading conditions [19–21]. However, the quantitative assessment of the resulting deformation still relies largely on external imaging, increasing cost and limiting portability and real-time feedback.

An approach to overcome this limitation is the integration of sensing elements directly within the device. Fiber-optic sensors have emerged as a promising solution due to their high sensitivity and immunity to electromagnetic interference [22,23]. Based on this approach, recent platforms combine pneumatic actuation with embedded fiber optic sensing, creating hybrid systems that deliver controlled deformation while simultaneously measuring stretch [24].

However, previous fiber-optic stretch devices have generally been limited to strain ranges below those required for physiological studies, with consistent operation rarely exceeding 2% [24]. Their performance under dynamic loading has also shown reduced repeatability. These limitations are especially relevant in cardiac mechanics studies, where experimental protocols require cyclic deformations in the 0–5% range and stable measurements with a sufficient signal-to-noise ratio to detect small tissue responses.

In this context, this study introduces a stretch device that builds on these advances by embedding a functionalized optical cavity inside a biocompatible polydimethylsiloxane (PDMS) membrane. Controlled deformation is achieved by modulating the air pressure within the cavity, enabling precise and uniform strain application to a biological tissue sample. To enhance measurement accuracy, an innovative optical fiber-based sensing technique is employed, where variations in light intensity are directly correlated with surface displacement. This mechanism is intrinsically linked to the gradual degradation of the total internal reflection (TIR) condition. Several optical fiber sensors have recently exploited the TIR degradation principle in other contexts, including rapid temperature variation detection [25], and wearable for biomechanical motion tracking [26]. While these studies highlight the versatility of TIR-based sensing across motion and thermal monitoring, the present device uniquely embeds this principle into a pneumatically actuated PDMS platform specifically tailored for dynamic tissue deformation studies.

Designed to measure micrometric displacements associated with cardiomyocyte contraction, both during externally applied stimulation and under spontaneous activity, the system allows real-time measurements without removing the sample from the incubator, thereby preserving controlled conditions of temperature and culture medium. Optical fiber sensing enables in situ monitoring without interfering with the culture. Reproducibility between devices is facilitated by the similarity of the optical path, with small variations in membrane thickness compensated by electronic calibration. These characteristics support closed-loop experiments in which mechanical stimulation can be adapted according to the measured tissue response.

To optimize the device, computational modeling was performed using COMSOL Multiphysics, enabling accurate prediction and verification of deformation responses under specific pressure conditions. In addition, custom electronics were developed and tested to ensure reliable performance and provide stable data acquisition. Together, these advances overcome the primary limitations of earlier designs, resulting in a cost-effective, biocompatible, and versatile solution for tissue deformation studies.

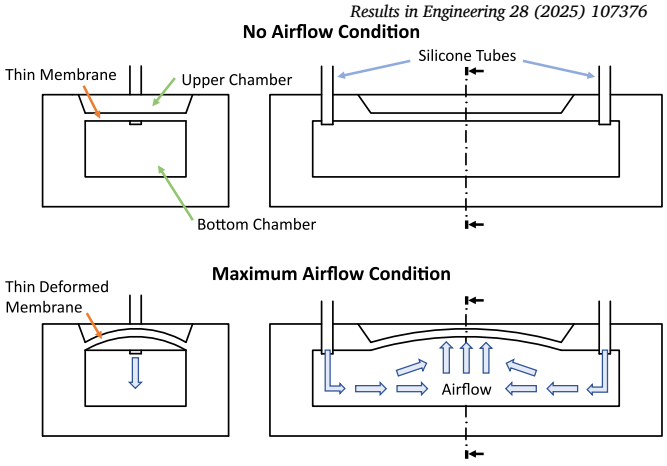

Fig. 1. Simplified scheme of the mechanical operation of the device, showing transverse (left) and longitudinal (right) section of the device under two operating conditions. No airflow condition (top): the lower chamber remains without air injection and the membrane is undeformed. Maximum airflow condition (bottom): air injection into the lower chamber produces maximum membrane deformation.

This work represents a significant advance in stretch technologies for biomedical applications, offering robust and high-sensitivity measurements. By addressing the key constraints of current systems, the proposed sensor improves precision, adaptability, and ease of use. Its innovative design positions it as a valuable tool for advancing tissue engineering research, enabling real-time exploration of dynamic tissue responses in biomedical studies.

2. Design and function of the stretching device

2.1. Physical and functional characteristics

To control tissue deformation, a custom-designed microfluidic device was fabricated. Given the specific application of this system, the design was made in accordance with the recommendations provided by experts in the field. These covered both dimensions, defined based on standard measurements reported in studies involving excised cardiac tissues [6,27], and materials, chosen to ensure compatibility with the experimental conditions and physiological constraints of the system.

The base material selected for the system was PDMS, chosen for its biocompatibility, transparency, and elasticity properties, which make it highly suitable for applications in biosensors and stretchable devices [28,29]. The device was composed of three main elements (Fig. 1): (i) a thin and flexible top layer, designed with an optimized thickness to withstand applied pressures while maintaining its deformation capacity; (ii) an internal cavity configured through COMSOL simulations to ensure uniform and precise deformation, maximizing stability and reproducibility; and (iii) thick side walls and a base layer that provide structural rigidity and prevent unwanted deformation in non-stretchable areas.

The device includes two air ports for input and output, connected to silicone tubes, allowing integration with a pneumatic system that injects controlled pressure (p). This design facilitates the generation of deformations in the top membrane, which is directly correlated with predefined stretch values. The thickness of the top layer was carefully selected to resist pressure without cracking while remaining thin enough to allow optical detection of the displacement within the deformation range required for cardiac applications.

With regard to deformation measurement, the design of the sensing mechanism started by identifying the optical property to be monitored. In this case, the variation in light intensity was chosen, an approach

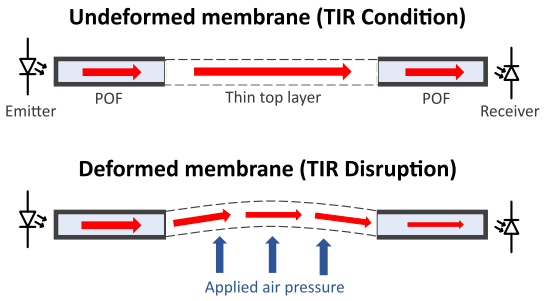

Fig. 2. Working principle diagram of the stretching device. The schematic illustrates only the thin upper PDMS membrane, which is the deformable region of the device. Under undeformed conditions (top), light propagates along the PDMS membrane via optical fibers maintaining TIR. When air pressure is applied (bottom), the resulting membrane deformation disrupts the TIR condition, altering the optical path. Narrow arrows represent reductions in the amount of transmitted light, indicating optical losses directly correlated with membrane deformation.

widely employed in optical fiber devices [30]. This variation could be achieved by altering the optical path, either by introducing discontinuities or deforming it. For this design, the optical path deformation approach was selected, leveraging the flexibility of the upper membrane. When the membrane deforms, the internal light path is altered, reducing the light reaching the receiver and thereby allowing a precise measurement of the induced stretch directly related to the movements of this membrane (Fig. 2).

The operation of the device was straightforward and yet effective 1. The tissue that was going to be deformed was placed on the thin upper layer of the upper cavity, and the two ends of the plastic optical fiber (POF) were precisely aligned with the flexible PDMS membrane. This membrane was designed as a thin layer to facilitate deformation according to stiffness criteria reported in the literature, while keeping its thickness close to the diameter of the optical fiber core to improve light coupling. Air was injected into the bottom cavity through the tubes, causing the upper membrane to raise and stretch the attached tissue, such as cardiac slices. This deformation altered the optical path of the light injected from the emitter, modifying the amount of light reaching the core of the receiving optical fiber. Consequently, the captured light intensity was directly related to the deformation experienced by the tissue.

Basically, in the absence of applied pressure, the membrane preserves the Total Internal Reflection (TIR) condition, allowing for maximum transmission of light. The critical angle for TIR [31] is defined as:

$$\theta_c = \arcsin\left(\frac{n_{\text{air}}}{n_{\text{PDMS}}}\right) \tag{1}$$

where $n_{\text{air}} \approx 1.0$ and $n_{\text{PDMS}} \approx 1.41$ at visible wavelengths [32]. The refractive index of PDMS exhibits only minor dispersion across the visible spectrum (variations below 0.01 between 500–800 nm), ensuring stable optical performance for the chosen source wavelength (see Section 2.3.2). As pneumatic pressure is introduced and the flexible layer deforms, the movement of the membrane (δ) modifies the incidence angle of the guided rays. As the effective angle approaches or falls below θ_c, the TIR condition is gradually compromised, leading to a reduced light transmission through the membrane and a decrease in the intensity detected at the receiver end. The transmitted optical intensity (I) can be expressed as $I(p) \approx I_0 e^{-\alpha \cdot \delta}$, where α is an effective attenuation coefficient. The mechanical deflection $\delta(p)$ follows the mechanics of thin elastic membranes under uniform pressure. According to classical plate theory [33], the central deflection scales with device geometry and material properties as:

$$\delta(p) \propto \frac{p w^4}{E t^3}, \tag{2}$$

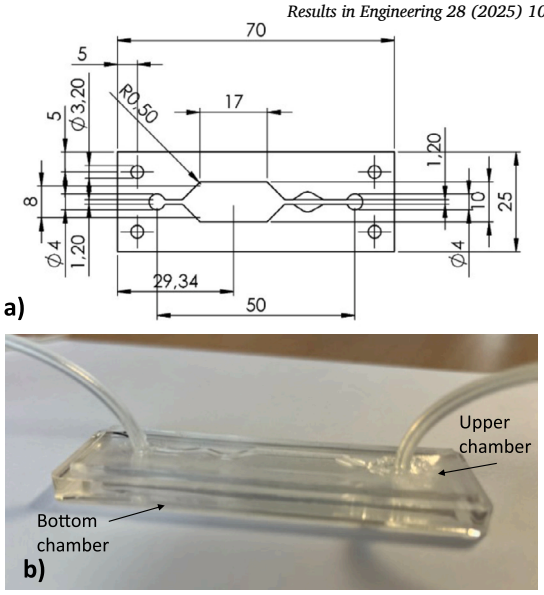

Fig. 3. (a) Schematic diagram with dimensions (in mm) showing the layout and geometry of the device. (b) Image of the fabricated device illustrating the upper and bottom chambers with tubing connections for air injection.

where w is the width of the deformable region, t is the membrane thickness, and E the Young's modulus whose value is taken from [34]. Consequently, the transmitted optical power is linearly converted by the photodiode into an electrical signal, such that the RMS output voltage is directly proportional to the transmitted intensity.

This formulation establishes a relationship between applied pneumatic pressure, membrane deformation, and electrical output, which was subsequently validated experimentally.

2.2. Fabrication methodology

The device consisted of two chambers with identical geometries: a lower chamber that houses the airflow and induced deformation of the thin upper PDMS layer, and an upper chamber that accommodated the tissue sample (Fig. 3b). In order to provide structural rigidity and to ensure that deformation is restricted to the thin upper membrane, the base and side walls of the device were fabricated with a greater thickness. The overall size of the device was designed to match the standard dimensions of a standard microscope slide (25 x 75 mm). This allowed for seamless integration with any fluorescence microscope slide holder, enabling direct evaluation of the tissue sample. The device was entirely fabricated using PDMS (SYLGARD™ 184 Silicone Elastomer) due to its biocompatibility and versatile fabrication properties. It was cast in an aluminum mold with a specific geometry (Fig. 3a), and the two blocks were bonded together by oxygen plasma treatment, which activates the surface for strong adhesion.

2.3. Optoelectronic system development

2.3.1. Electronic design and feedback control loop

The electronic system developed to control the device and allow the characterization of tissue deformation consisted of two main parts, an analog block and a digital block (Fig. 4). These subsystems operated in an integrated manner to facilitate signal acquisition, processing, and analysis.

The analog block was responsible for signal transmission and reception, incorporating a feedback mechanism to regulate the operating point and ensure stability. This block directly represented the operating principle of the system. It consisted of an optocoupler (emitter and receiver) whose terminals were connected via an optical path formed by the optical fiber emerging from each component, along with the

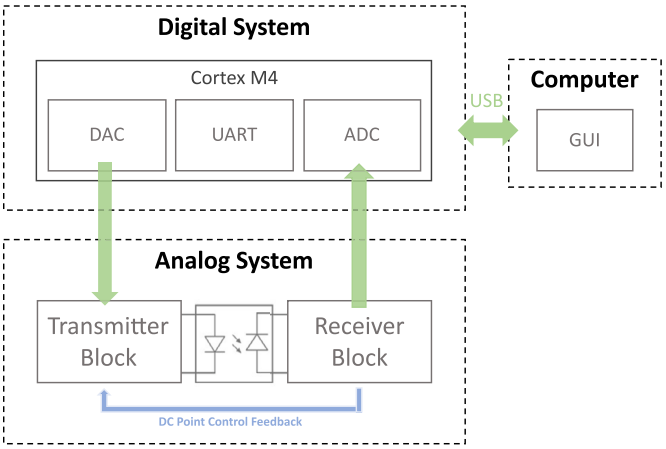

Fig. 4. Schematic diagram of the electronics for the device. Showing an analog block for optical emission and detection, and the digital block for real-time signal processing and data transmission.

upper layer of the device that interrupts the path between these two terminals. The digital block, implemented within a Cortex-M4 microcontroller, performed data conversion and managed serial communication via a UART interface. Data were transmitted from the microcontroller to an external computer or peripheral device through a UART-to-USB interface, enabling real-time monitoring, analysis, and visualization via a graphical user interface (GUI). In addition, it generated the signal applied to the stretch system using the transmitter block of the analog subsystem, ensuring controlled and stable optical excitation.

Fig. 5 illustrates the detailed diagram block of the analog section of the platform. The input signal (V_{IN}) generated by the digital system was a sinusoidal waveform with 125 Hz frequency and 1 V amplitude superimposed on a 1.5 V DC offset. This signal was obtained using one channel of the digital-to-analog converter (DAC) integrated into the microcontroller of the Nucleo-L452RE-P (STMicroelectronics) development board. First, its DC component was removed through a coupling capacitor. Next, a new DC offset adjusted by the feedback control loop was added. The resulting signal drove the emitter LED connected at one end of the optical fiber.

At the opposite end of the fiber, the receiver photodiode converted the optical intensity into a current, which was translated into a voltage across a load resistor connected to its anode. This voltage was then buffered to enable its split into two separate paths. In one path, the voltage levels were adjusted to match the input range of the microcontroller's analog-to-digital converter (ADC) using a conditioning stage that amplified only the AC component of the signal. The stage gain was set to optimize utilization of the dynamic range of the signal.

In the second path (highlighted in blue in Fig. 5), the signal entered a feedback control loop, where a stage of integral control processed the error signal, defined as the difference between a predefined reference voltage ($V_{control}$) and the filtered DC component extracted from the final signal output. Through this mechanism, the system continuously adjusts the DC level of the intermediate signal (V_f) to ensure that the excitation signal applied to the emitter (i_{Led}) contains the appropriate DC component. This regulation guarantees that the signal at the photodiode output (V_{Phot}) remains consistently stabilized at a 1.5 V DC level. The overall architecture enabled precise tracking of light intensity variations induced by membrane deformation, ensuring high sensitivity and stability for optical sensing purposes. In addition, the feedback loop stabilized the LED output, compensating for potential drifts due to temperature or bias variations and ensuring consistent optical excitation during the experiments.

Therefore, the generated waveform served as a reference for evaluating the system response at a specific position induced by the air injected. By analyzing the characteristics of the output waveform (V_{OUT}), it was possible to quantify the stretch experienced by cardiac tissue, providing a direct assessment of its mechanical behavior under controlled conditions.

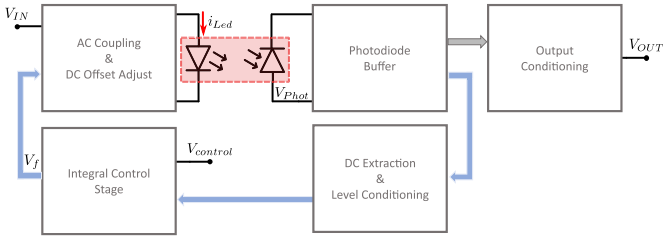

Fig. 5. Block representation of the analog electronics developed for optical conditioning. The system drives the emitter and processes the photodiode output through amplification stages and a feedback control loop that dynamically adjusts the emitter bias to maintain a stable operating point.

2.3.2. PDMS integrated optical path design

To determine the most suitable optocoupler pair for the optical sensing system, a spectral characterization of the light path was performed. A broadband visible light source (HL-2000, Ocean Optics) and a high-sensitivity spectrometer (QE6500, Ocean Optics) were used to measure the light intensity reaching the receiver through the top layer. The resulting transmission spectrum revealed two main intensity peaks centered around 660 nm and 760 nm (Fig. 6). These values fall within the red region of the visible light spectrum, which corresponds to the wavelengths with the highest transmission efficiency under baseline (non-deformed) conditions.

Based on these results, a FC300T optocoupler pair was selected. This component operated with peak emission around 660 nm, aligning well with an excellent transmission region identified experimentally, and delivered about 150 μW of optical power at a drive current of 20 mA. In addition, the optocoupler included an integrated optical fiber fixation system, which facilitated alignment and ensured optimal light coupling throughout the experiments. A plastic optical fiber (Eska Mega) with a 1 mm core diameter was used, chosen to better match the thickness of the upper PDMS layer and improve optical coupling efficiency.

3. Experimental and simulation methodology

For experimental validation, a two-step characterization approach was implemented. First, the maximum deformation range was determined by measuring the vertical displacement of the upper membrane under different applied pressures, within the operating limits of the device. In a second step, the relationship between the membrane deformation and the electrical output signal was experimentally established. This two-stage strategy was adopted to simplify the measurement procedure and to allow a direct comparison between the experimentally obtained pressure–height relation and the deformation profile predicted by the COMSOL simulation model.

3.1. Experimental setup

The experimental setup used to test the prototype device is illustrated in Fig. 7. The system was configured to enable optical monitoring of the vertical deformation of the thin PDMS membrane under controlled pneumatic actuation. The cut ends of two optical fibers were placed on opposite sides of the membrane using a custom 3D-printed mount attached to a micropositioning stand for fine alignment. The silicone tubing connected the internal cavity of the device to an external pressure source, allowing precise modulation of internal air pressure and deformation of the membrane.

For device characterization, additional instrumentation was used, including an independent optical tracking system. A high-resolution camera was placed along the same axis as the optical fibers, providing a

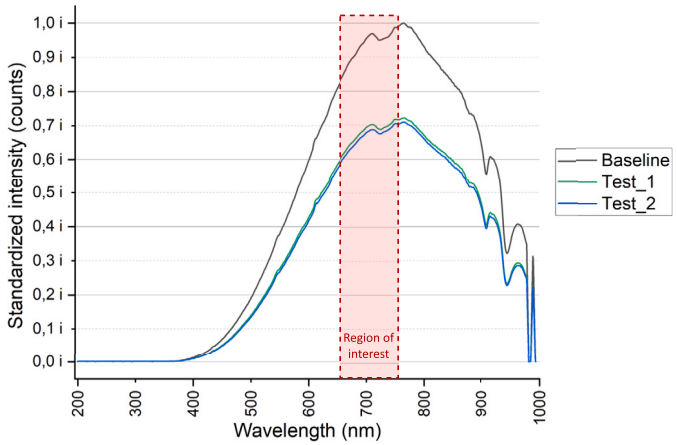

Fig. 6. Optical path characterization curve. Gray: undeformed membrane situation (baseline); green and blue: deformed membrane tests. The measured light intensity was standardized and plotted against wavelength. A shaded red area highlights the region of interest (650–760 nm), which corresponds to the range of maximum light transmission and guided the selection of the optocoupler pair.

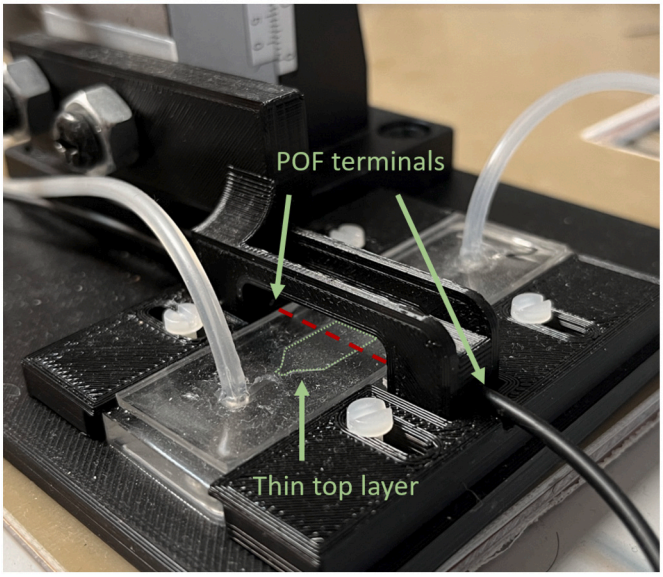

Fig. 7. Experimental setup configured to test the prototype device. The cut ends of the optical fiber are precisely aligned with the thin, deformable PDMS membrane by means of a custom 3D-printed mount attached to a micropositioner stand. Silicone tubing connected to the device modulates the internal air pressure, enabling controlled deformation. The dashed red line indicates the optical path from the LED emitter to the photodiode detector during operation.

side view of the device and enabling direct observation of the vertical displacement of the membrane during actuation. To facilitate accurate visual tracking, the camera feed was projected onto a screen, allowing for enlarged inspection of the membrane profile. A surface-mounted resistor (0402 package) was placed within the same imaging plane and used as a reference scale. This approach enabled a consistent estimation of membrane deformation by relating the apparent displacement to the calibrated reference using proportional scaling.

In addition, a pressure sensor (All Sensors, Amphenol) was integrated into the setup through a branch of the pneumatic circuit upstream of the device. This configuration enabled direct monitoring of pressure variations within the bottom chamber, just beneath the sensing membrane. The pressure variations monitored by the sensor were directly related to the deformation experienced by this membrane. The sensor module was controlled through an I^2C interface managed by the digital subsystem, enabling continuous real-time monitoring of applied pressure during the experimental procedure. Although not required for regular device operation, this component was essential to establish the pressure-dependent behavior of the mechanical deformation and the electrical output. Combining these datasets, a final correlation was obtained between membrane deformation and voltage output, which served as the basis for the operation of the stretch device.

All experiments were carried out in a temperature-controlled laboratory (20–25 °C), ensuring stable operation of the PDMS layer, optical fibers, and photodetector. In practical use, the device is intended to operate inside standard cell-culture incubators at 37 °C, where temperature is tightly regulated, so thermal drifts are negligible.

3.2. Numerical modeling and validation for membrane characterization

To complement the experimental approach, a finite element model of the device was developed using COMSOL Multiphysics. The simulation focused on the mechanical behavior of the upper PDMS membrane under applied pressure, with the goal of accurately estimating its vertical deformation. This modeling strategy was especially useful because of the difficulty in precisely controlling the membrane thickness during the fabrication process, which could introduce uncertainty in the experimental measurements. In this analysis, Young's modulus was selected as a key parameter because it strongly influences the deformation response of the membrane in a manner comparable to geometric dimensions, whereas other properties, such as Poisson's ratio [35], remain more constant and were therefore not studied in detail in this study.

The numerical model was configured to replicate the actual geometry of the device, including boundary conditions and material properties. By simulating the membrane response to incremental pressure loads, the model provided a detailed prediction of the pressure–deformation relationship, which could be directly compared with experimental measurements. The deformable region was modeled as a rectangular membrane with fixed perimeter boundary conditions, subjected to a uniform pressure on its bottom surface that induced vertical upward deformation. This comparison served as a validation step for the accuracy of both the model and the optical measurement system used during characterization.

In addition to supporting the interpretation of the experimental data, the COMSOL model enabled systematic parametric analysis. A key variable explored was Young's modulus of PDMS, which varies significantly depending on the base-to-curing agent ratio used during preparation. By adjusting this parameter in the simulation, it was possible to predict how variations in fabrication conditions would affect the mechanical response of the membrane, and consequently the behavior of the device. Thus, this modeling framework offered a valuable tool for optimizing structural design and anticipating performance variability due to material or geometric tolerances.

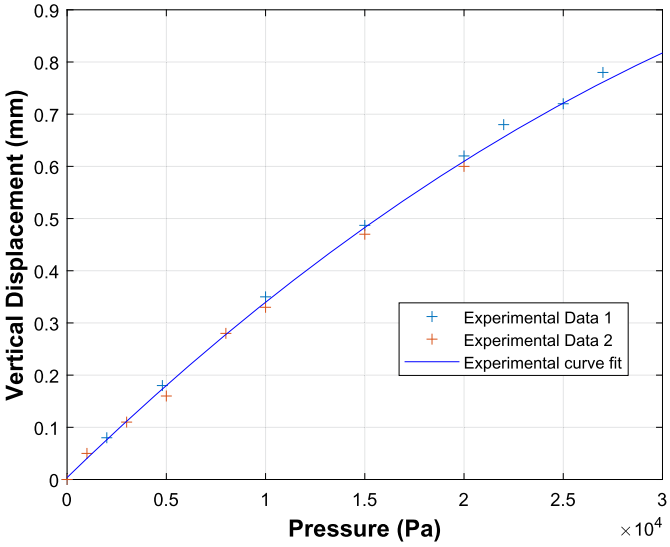

Fig. 8. Relationship between applied pressure and vertical displacement. The plot shows two experimental datasets obtained from independent trials, together with the averaged polynomial fit. The resulting curve captures the overall trend of the mechanical response of the device over a broad pressure range.

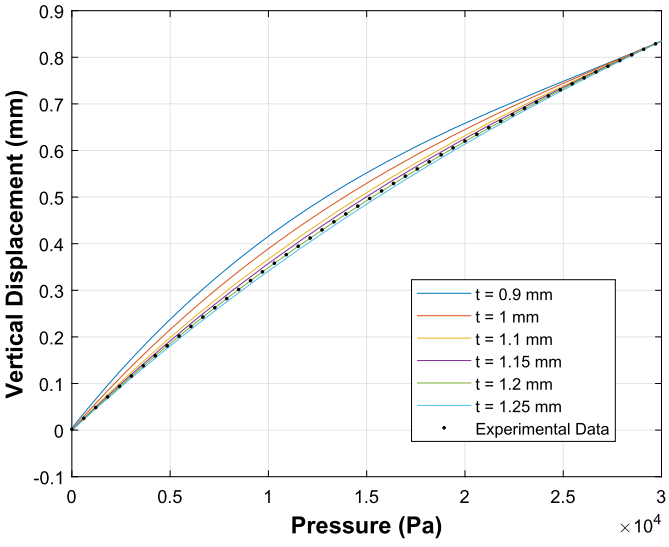

Fig. 9. Membrane deformation simulated in COMSOL for different PDMS layer thickness values (t), compared with experimental data (dotted line). The closest agreement is found for a thickness of 1.2 mm (green line).

4. Results and discussion

Using the experimental setup described above, validation tests were performed to characterize the behavior of the device. These experiments resulted in two main datasets: the first relates the applied pressure to the mechanical displacement of the system, while the second relates the pressure to the electrical output signal provided by the acquisition system. To provide a quantitative measurement of the electrical signal, the root mean square (RMS) value was used, which was digitally calculated in the microcontroller from the signal received at the input of the ADC.

These two datasets are complementary and are analyzed jointly. Pressure-displacement measurements establish the mechanical response of the PDMS membrane and enable validation against the FEM predictions. Pressure-voltage measurements quantify the optical and electronic transduction of that deformation, assessing linearity, dynamic range, and repeatability. Together they provide a coherent description of device operation, from the pneumatic input through structural deformation to the electrical readout, linking the mechanical and sensing subsystems.

4.1. Mechanical characterization and model validation

Initial experimental validations focused on establishing the relationship between membrane displacement and a range of applied pressures from 0 to 27 kPa. Fig. 8 shows two datasets obtained from this type of experiment. A separate polynomial fit was performed for each dataset, and the average of these fits was calculated to produce a representative curve that accurately captured the overall behavior observed in the experimental data. This averaged curve is also shown in the figure, illustrating the quality of the fit relative to the measured data. The pressure range covered by the second dataset is slightly lower, as the measurements were stopped once the transmitted light reaching the photodiode was no longer detected or when unexpected behavior was observed, such as a sudden drop in the signal amplitude unrelated to the applied pressure.

To better understand the behavior of the fabricated structure, a series of simulations was carried out using a finite element model implemented in COMSOL Multiphysics. These simulations involved varying the thickness of the top PDMS layer (t), allowing a detailed comparison with the experimental measurements. As shown in Fig. 9, the response observed experimentally closely matches the simulation for a thickness of the top PDMS layer of 1.2 mm. This agreement validates the predictive capability of the model while also indicating that this value corresponds to the effective thickness of the fabricated membrane within the expected manufacturing tolerances. Since the precise thickness of the top PDMS layer is difficult to control during fabrication, this combined approach of simulation and experiment provides a reliable estimation of the actual device geometry

In the simulations, a Young's modulus of 3.75 MPa was used, consistent with values reported in the literature for Sylgard 184 when mixed in a 10 to 1 ratio between the base and the curing agent [36]. This formulation yielded a stiffer PDMS suitable for applications requiring accurate mechanical behavior.

The comparison in Fig. 9 revealed the critical influence of geometric precision during fabrication. Even small deviations, on the order of tens of microns, in the thickness of the top PDMS layer can lead to noticeable differences in the mechanical response of the device. This sensitivity highlights the need for careful control of the manufacturing process to ensure repeatable and consistent performance.

4.2. Optoelectronic response and repeatability

In this experiment, the applied pressure was increased progressively until the optical coupling through the top thin PDMS layer was no longer functioning properly, at which point data collection was excluded. This behavior was used to define the upper pressure limit for each run. Values slightly above 30 kPa were reached before the device behavior became unstable. A total of five complete pressure sweeps were performed to evaluate the repeatability of the device.

The analog signal was sampled at a rate of 25 kHz using the 12-bit ADC of the microcontroller. The samples were stored in memory as 16-bit variables and transmitted to a computer via UART in data packets of 6000 bytes, covering a time window of 120 ms. Given an input signal frequency of 125 Hz, this represents 15 full cycles of the measured signal. The RMS value was calculated from each of these segments using MATLAB, and the resulting value was saved in a text file along with the corresponding pressure readings.

As shown in Fig. 10, the measured RMS voltage as a function of the applied pressure in the pneumatic system exhibits a trend that is approximately linear, particularly for pressures above 5 kPa. This linearity indicates that the electrical output remains stable and consistent within the expected operating pressure range.

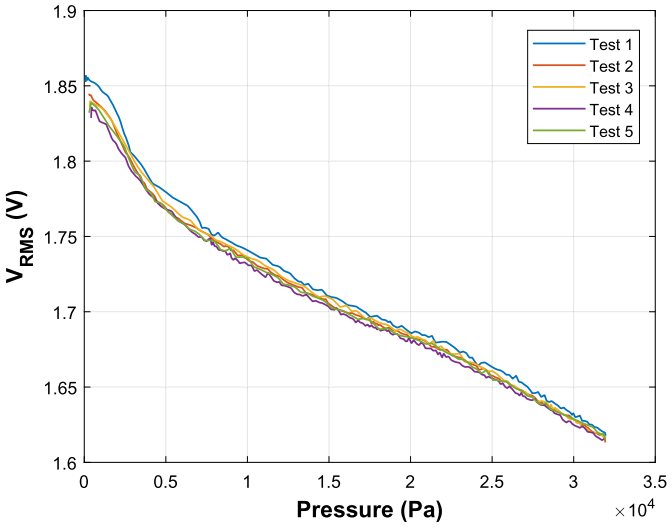

Fig. 10. RMS voltage measured across five pressure sweeps. Data collection was stopped beyond the point where the optical signal was no longer effectively transferred through the thin PDMS layer. The observed consistency across multiple sweeps indicates good repeatability of the electrical output.

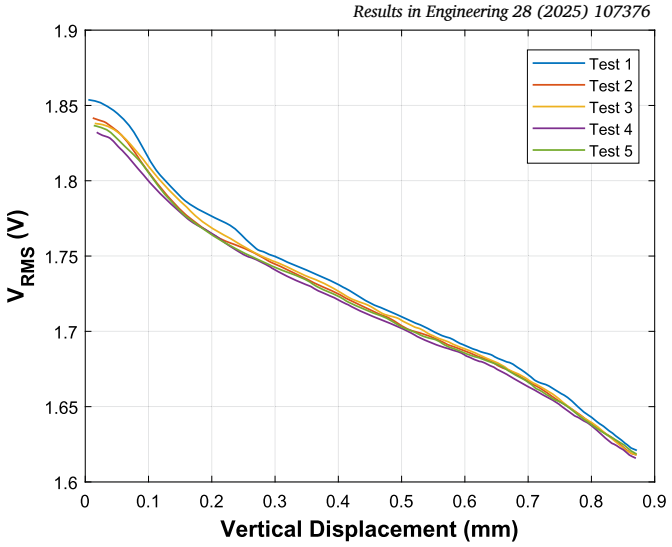

Fig. 11. RMS voltage measured at the output of the system as a function of the vertical displacement of the top PDMS layer. The five curves correspond to independent repetitions of the experiment.

Following pressure-based experiments, a second set of tests was conducted to directly relate the vertical displacement of the top PDMS layer to the RMS voltage measured at the output. As shown in Fig. 11, five independent tests were performed for a similar range of displacements. The data presented corresponds to a smoothing of the raw data by a moving average. The resulting electrical response exhibited a consistent and monotonic increase with displacement. Despite minor variations between curves, the trend was clearly maintained throughout all iterations, suggesting stable behavior and good agreement between mechanical deformation and the voltage output signal.

To quantify this consistency, the coefficient of variation was calculated at each displacement value in the five repetitions. The results show a median value of 0.19% and a maximum below 0.44%, indicating excellent repeatability and minimal variability between measurements, confirming its suitability for quantitative displacement monitoring in stretching applications. Although the present protocol involved only monotonic pressure sweeps, precluding a full load–unload hysteresis analysis, an apparent inter-cycle hysteresis was estimated by comparing the RMS values at the same initial pressure across repeated sweeps. The resulting value was approximately 5% of the measurement span, indicating that hysteresis is negligible within the tested range.

This characterization validates an operating window up to approximately 30 kPa, where the response remains monotonic and reproducible. At higher pressures the device does not fail mechanically; instead, excessive curvature of the top PDMS layer imposes an optical coupling limit that leads to irregular signal behavior. A more detailed analysis of this phenomenon is presented in Section 4.5.

4.3. Sensitivity analysis of voltage-to-stretch relationship

To evaluate the performance of the system in terms of stretching capabilities, vertical displacement measurements were converted into stretch ratio values using analytical models that describe the mechanics of thin membranes under applied pressure. In the presented device, stretch arises directly from the pneumatic deformation of the PDMS top membrane, which is clamped at its perimeter and deforms freely in the central region without requiring external adhesion. The formulations presented by Xiang et al. [33] and further developed by Pakazad et al. [37] establish a relationship between the central deflection of the membrane and the resulting strain in the film plane, which was adapted here to the geometry of the device. In particular, the model parameter corresponding to the width of the deformable top membrane was defined as $L_0 = 8$ mm, according to the device dimensions shown in Fig. 3. This definition follows the nomenclature introduced by Pakazad et al. [37], where the original length of the membrane cross section is given by $L_0 = 2R$, with $R = 4$ mm. To clarify terminology, the terms strain and stretch were used interchangeably to describe the relative elongation of the membrane, since the deformations remain small (in relative terms, typically in the range 0–5%) [33].

Fig. 12 presents the measured RMS voltage as a function of the stretch calculated for five independent repetitions. The relationship between both variables tended to become approximately linear for stretch values greater than 0.5%. A linear fit applied to this range led to the expression $V_{\mathrm{RMS}} = -0.0425 \cdot \mathrm{Stretch} + 1.7517$, with a coefficient of determination $R^2 = 0.9972$, confirming the strong linearity of the response. The inset in the upper right corner shows a closer view of the 1–2% stretch interval to improve clarity and facilitate interpretation of the results.

The sensitivity of V_{RMS}, defined as the slope of the voltage-to-strain curve, was first obtained considering the whole strain range: -0.0723 $V/\%$. However, since a single global value hides the clear change in the slope across the range, the sensitivity was recalculated in two intervals, leading to: -0.2078 $V/\%$ for the 0-0.5% strain interval and -0.0451 $V/\%$ for the 0.5-3% strain interval. This interval-wise analysis makes explicit the steeper slope at low strains and provides coefficient values for accurate calibration in each region.

Such behavior can be understood in terms of the optical losses associated with bending-induced modifications of the incidence angles within the fiber. When the membrane curvature is small, a significant fraction of guided rays propagate close to the critical angle, so even slight deformations redistribute their incidence and progressively compromise TIR. This leads to a more pronounced loss of transmitted intensity and, consequently, to an apparently higher sensitivity. As curvature increases further, most of these rays have already been coupled out into cladding or leaky modes, reducing the incremental effect of additional deformation and giving rise to a lower sensitivity regime [26,30].

Statistical analysis of signal variation confirms the high repeatability of the system, with a median coefficient of variation below 0.5% for all measurements. These results validate the system's capacity to translate the stretch induced on the upper membrane into an electrical output with both precision and robustness.

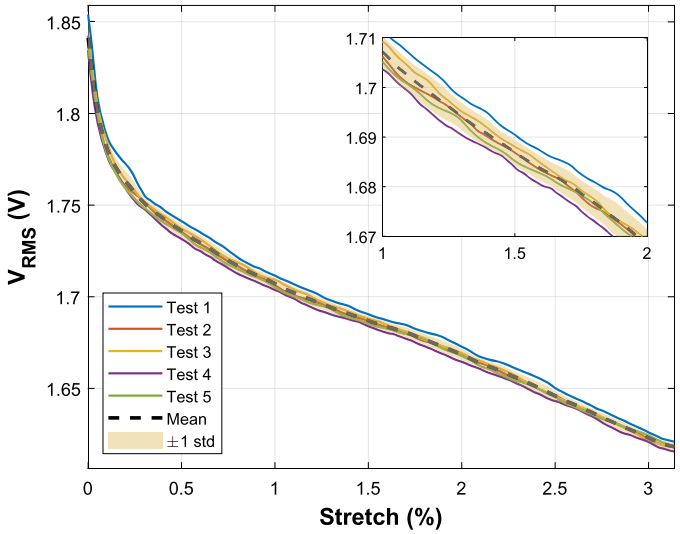

Fig. 12. RMS voltage measured at the output of the system as a function of induced strain (%) for five independent tests. The dashed black line denotes the mean response and the orange shading indicates ±1 standard deviation. The inset in the upper right corner provides a closer view of the 1–2% stretch range to improve clarity and facilitate interpretation of the results.

4.4. Applicability to tissue engineering

The mechanical behavior of the device under controlled deformation conditions suggests its suitability for biomedical applications, where precise mechanical stimulation patterns are essential. One of the most relevant contexts is cardiac tissue engineering, with cardiomyocytes in engineered heart tissues able to respond to mechanical cues. *In vitro* studies commonly apply cyclic strains of at least 5% to mimic physiological conditions and promote cardiomyocyte alignment, maturation and functional development [38,39].

In the present work, the developed system exhibited consistent and repeatable behavior within a stretch range exceeding 3% (Fig. 12). Although this value remains slightly below the typical 5% used in cardiomyocyte stimulation protocols [40], it still falls within a biomechanically relevant range for cardiac applications. Moreover, the resolution of the device in the 0–5% interval also makes it suitable for stimulating other soft tissues, such as skeletal muscle or vascular tissue, where patterned mechanical signals are crucial to guide cell differentiation and tissue development [41,42].

The sensing platform combines simplicity, ease of use, and biocompatible materials, making it suitable for integration into dynamic culture systems. Its reliable signal transduction within a physiologically relevant strain range supports its use for both real-time monitoring and active feedback control on biomedical platforms.

In addition, the sensing system offers practical advantages, such as low fabrication costs and streamlined electronic instrumentation. The compact design and limited setup requirements further enhance its portability, facilitating its adoption across different laboratory environments. Together, these characteristics position the sensor as a versatile and accessible platform for biological studies and functional tissue engineering applications.

In comparison with existing stretch platforms, Cytostretch [17] achieves a wider strain window but exhibits a nonlinear response over that interval, whereas the present system provides a near-linear, repeatable electrical readout up to ~3% and a mechanical margin to ~5%, with the current upper bound set by the optical pathway. Compared with the optical PDMS sensor described in [24], the presented platform extends the experimentally measured stretch window beyond ~1.5%. Vacuum-driven pneumatic compression devices [19,21] reach somewhat higher strains but rely on external imaging for deformation tracking, which complicates closed-loop operation. In contrast, our device integrates actuation and sensing and delivers a direct electrical readout suitable for real-time feedback. Targeted improvements in light delivery and detection are expected to extend the achievable strain range while preserving linearity and repeatability.

Although no biological experiments are reported in the present work, the device was designed with dimensional and operational specifications directly compatible with the standard cardiac and soft tissue stimulation protocols reported in previous studies [43]. Therefore, the present results establish the technological basis for subsequent validation in excised tissues, which constitutes the next step of this work.

4.5. Operational range and system limitations

A limitation was identified with respect to the operational range of the optical detection system. Although the device is mechanically capable of achieving vertical displacements sufficient to induce target stretch values of up to 5%, corresponding to approximately 1.1 millimeters of central deflection under an applied pressure of 40 kPa, the optical signal becomes unstable beyond approximately 30 kPa. This behavior has an optical origin. As the membrane bends, the surface normal rotates, and the incidence angles at the PDMS/air interface move beyond the condition for total internal reflection. Guided power is progressively lost into leaky and cladding modes or scattered outside the acceptance cone of the receiving fiber, and the remaining signal is governed by weak parasitic paths that respond strongly to minute pressure fluctuations or micromotions. This mechanism explains the nonmonotonic excursions observed in the RMS voltage at high pressure and establishes the effective performance limit of the system. In this range, the photodetector no longer receives a consistent light signal, resulting in a deterioration of the measurement accuracy. As a result, the current performance limit of the system is imposed by the optical subsystem rather than by the mechanical structure. Addressing this constraint will be essential to fully exploit the deformation capabilities of the platform in future implementations.

Several strategies are proposed here to overcome this limitation and extend the functional range of the system. First, modifying the geometry of the deformable membrane, for example by reducing the width of the upper PDMS layer, would increase the curvature for a given displacement, enabling the desired stretch at lower pressures. However, this approach would reduce the available area for tissue samples and would require a further evaluation of the optical performance under these modified conditions. Second, upgrading the optical components by employing a more powerful or focused light source and a more sen-

sitive detection unit could enhance signal stability at higher deformation levels. Lastly, redesigning the optical path through internal guiding structures or integrated waveguides could significantly improve transmission efficiency and extend the reliable measurement range.

5. Conclusions

The developed optical fiber sensing system exhibits stable and repeatable mechanical and electrical responses within a strain range of 0% to 3%. Experimentally, a strong linear correlation was confirmed between applied pressure, vertical displacement, and output voltage. Finite element simulations validated these findings, identifying the effective thickness of the top membrane as 1.2 mm and highlighting the importance of precise control during the device fabrication process.

The use of optical fiber as the sensing element provides inherent immunity to electromagnetic interference and reduces susceptibility to temperature variations, ensuring accurate measurements in challenging environments. In addition, the low fabrication cost, simplicity of electronic instrumentation, and compact nature of the entire experimental setup enable portability and adaptability across different laboratory settings.

CRediT authorship contribution statement

Antonio Velarte: Writing – review & editing, Writing – original draft, Software, Methodology, Investigation, Conceptualization. **Andrea Sannino:** Writing – original draft, Software, Methodology, Investigation, Conceptualization. **Aranzazu Otin:** Writing – review & editing, Supervision. **Beatriz Santamaría:** Writing – review & editing, Resources. **José Ignacio Artigas:** Writing – review & editing, Supervision, Resources. **Esther Pueyo:** Writing – review & editing, Supervision, Funding acquisition.

Declaration of generative AI and AI-assisted technologies in the writing process

During the preparation of this work the authors used ChatGPT in order to check and improve spelling and grammar. After using this tool/service, the author(s) reviewed and edited the content as needed and take(s) full responsibility for the content of the publication.

Declaration of competing interest

The authors declare that they have no known competing financial interests or personal relationships that could have appeared to influence the work reported in this paper.

Acknowledgement

This study was supported by Gobierno de Aragón through project LMP94_21, and by Agencia Estatal de Investigación - Ministerio de Ciencia e Innovación through projects PID2022-140556OB-I00 and TED2021-130459B-I00, as well as by BSICoS group T39_23R and GEPM group T23_23R. Additional support was provided by *NEUROBIO-PIELTEC-CM* (Ref.: TEC2024/BIO-98) *of Madrid Regions: Integración de nuevas tecnologías organ-on-chip para el estudio de enfermedades cutáneas y neurodegenerativas, and by Instituto de Salud Carlos III* (*ISCIII*) *under the project PT23/00167 and the project TALES* (Ref.: PID2023-149403OB-I00).

Computations were performed using ICTS NANBIOSIS (HPC Unit at University of Zaragoza). We would like also to thank the Group of Optics, Photonics and Biophotonics (GOFB) of the Universidad Politécnica de Madrid (UPM) for the fabrication and development of the microfludic chips.

Data availability

Data will be made available on request.

References

[1] C.J.L. Murray, The global burden of disease study at 30 years, Nat. Med. 28 (10) (2022) 2019–2026, https://doi.org/10.1038/s41591-022-01990-1.

[2] G. Zeng, H. Wang, P. Cao, J. Zhao, L. Liu, H. Guo, Changing patterns of cardiovascular diseases and subtypes induced by kidney dysfunction among 25–64 years in China from 1992 to 2021, BMC Public Health 25 (1) (2025) 26, https://doi.org/10.1186/s12889-024-21183-4.

[3] M. Vaduganathan, G.A. Mensah, J.V. Turco, V. Fuster, G.A. Roth, The global burden of cardiovascular diseases and risk, J. Am. Coll. Cardiol. 80 (25) (2022) 2361–2371, https://doi.org/10.1016/j.jacc.2022.11.005.

[4] S. Chen, X. Lu, C. Zheng, J. Wu, H. Tang, X. Wang, Y. Tian, X. Cao, Y. Tian, R. Gu, et al., The impact of environmental factors on cardiopulmonary health, Biomed. Environ. Sci. 37 (12) (2024) 1349–1351.

[5] B. Chong, J. Jayabaskaran, S.M. Jauhari, S.P. Chan, R. Goh, M.T.W. Kueh, H. Li, Y.H. Chin, G. Kong, V.V. Anand, J.-W. Wang, M. Muthiah, V. Jain, A. Mehta, S.L. Lim, R. Foo, G.A. Figtree, S.J. Nicholls, M.A. Mamas, J.L. Januzzi, N.W.S. Chew, A.M. Richards, M.Y. Chan, Global burden of cardiovascular diseases: projections from 2025 to 2050, Eur. J. Prev. Cardiol. (2024) zwae281, https://doi.org/10.1093/eurjpc/zwae281.

[6] F.G. Pitoulis, S.A. Watson, F. Perbellini, C.M. Terracciano, Myocardial slices come to age: an intermediate complexity in vitro cardiac model for translational research, Cardiovasc. Res. 116 (7) (2020) 1275–1287, https://doi.org/10.1093/cvr/cvz341.

[7] M. Brandenburger, J. Wenzel, R. Bogdan, D. Richardt, F. Nguemo, M. Reppel, J. Hescheler, H. Terlau, A. Dendorfer, Organotypic slice culture from human adult ventricular myocardium, Cardiovasc. Res. 93 (1) (2012) 50–59, https://doi.org/10.1093/cvr/cvr259.

[8] F. Perbellini, S.A. Watson, M. Scigliano, S. Alayoubi, S. Tkach, I. Bardi, N. Quaife, C. Kane, N.P. Dufton, A. Simon, M.B. Sikkel, G. Faggian, A.M. Randi, J. Gorelik, S.E. Harding, C.M. Terracciano, Investigation of cardiac fibroblasts using myocardial slices, Cardiovasc. Res. 114 (1) (2018) 77–89, https://doi.org/10.1093/cvr/cvx152.

[9] S.A. Watson, A. Dendorfer, T. Thum, F. Perbellini, A practical guide for investigating cardiac physiology using living myocardial slices, Basic Res. Cardiol. 115 (6) (2020) 61, https://doi.org/10.1007/s00395-020-00822-y.

[10] C. Kong, Z. Guo, T. Teng, Q. Yao, J. Yu, M. Wang, Y. Ma, P. Wang, Q. Tang, Electroactive nanomaterials for the prevention and treatment of heart failure: from materials and mechanisms to applications, Small 20 (49) (2024) 2406206, https://doi.org/10.1002/smll.202406206.

[11] C. Fischer, H. Milting, E. Fein, E. Reiser, K. Lu, T. Seidel, C. Schinner, T. Schwarzmayr, R. Schramm, R. Tomasi, B. Husse, X. Cao-Ehlker, U. Pohl, A. Dendorfer, Long-term functional and structural preservation of precision-cut human myocardium under continuous electromechanical stimulation in vitro, Nat. Commun. 10 (1) (2019) 117, https://doi.org/10.1038/s41467-018-08003-1.

[12] Q. Ou, Z. Jacobson, R.R. Abouleisa, X.-L. Tang, S.M. Hindi, A. Kumar, K.N. Ivey, G. Giridharan, A. El-Baz, K. Brittian, B. Rood, Y.-H. Lin, S.A. Watson, F. Perbellini, T.A. McKinsey, B.G. Hill, S.P. Jones, C.M. Terracciano, R. Bolli, T.M. Mohamed, Physiological biomimetic culture system for pig and human heart slices, Circ. Res. 125 (6) (2019) 628–642, https://doi.org/10.1161/circresaha.119.314996.

[13] Y. Qiao, Q. Dong, B. Li, S. Obaid, C. Miccile, R.T. Yin, T. Talapatra, Z. Lin, S. Li, Z. Li, I.R. Efimov, Multiparametric slice culture platform for the investigation of human cardiac tissue physiology, Prog. Biophys. Mol. Biol. 144 (2019) 139–150, https://doi.org/10.1016/j.pbiomolbio.2018.06.001.

[14] K. Kroll, M. Chabria, K. Wang, F. Häusermann, F. Schuler, L. Polonchuk, Electromechanical conditioning of human iPSC-derived cardiomyocytes for translational research, Prog. Biophys. Mol. Biol. 130 (2017) 212–222, https://doi.org/10.1016/j.pbiomolbio.2017.07.003.

[15] F.G. Pitoulis, R. Nunez-Toldra, K. Xiao, W. Kit-Anan, S. Mitzka, R.J. Jabbour, S.E. Harding, F. Perbellini, T. Thum, P.P. De Tombe, C.M. Terracciano, Remodelling of adult cardiac tissue subjected to physiological and pathological mechanical load in vitro, Cardiovasc. Res. 118 (3) (2022) 814–827, https://doi.org/10.1093/cvr/cvab084.

[16] J. Kim, C. Won, S. Ham, H. Han, S. Shin, J. Jang, S. Lee, C. Kwon, S. Cho, H. Park, D. Lee, W.J. Lee, T. Lee, J.H. Lee, Increased susceptibility to mechanical stretch drives the persistence of keloid fibroblasts: an investigation using a stretchable PDMS platform, Biomedicines 12 (10) (2024) 2169, https://doi.org/10.3390/biomedicines12102169.

[17] N. Gaio, B. Van Meer, W. Quirós Solano, L. Bergers, A. Van De Stolpe, C. Mummery, P. Sarro, R. Dekker, Cytostretch, an organ-on-chip platform, Micromachines 7 (7) (2016) 120, https://doi.org/10.3390/mi7070120.

[18] F.G. Pitoulis, J.J. Smith, B. Pamias-Lopez, P.P. De Tombe, D. Hayman, C.M. Terracciano, MyoLoop: design, development and validation of a standalone bioreactor for pathophysiological electromechanical in vitro cardiac studies, Exp. Physiol. 109 (3) (2024) 405–415, https://doi.org/10.1113/EP091247.

[19] H. Peussa, J. Kreutzer, E. Mäntylä, A.-J. Mäki, S. Nymark, P. Kallio, T.O. Ihalainen, Pneumatic equiaxial compression device for mechanical manipulation of epithelial

cell packing and physiology, PLoS ONE 17 (6) (2022) e0268570, https://doi.org/10.1371/journal.pone.0268570.

[20] D. Jaworski, L. Hundsdorfer, E. Bastounis, I. Constantinou, StretchView – a multi-axial cell-stretching device for long-term automated videomicroscopy of living cells, Adv. Sci. 12 (9) (2025) 2408853, https://doi.org/10.1002/advs.202408853.

[21] J. Kreutzer, L. Ikonen, J. Hirvonen, M. Pekkanen-Mattila, K. Aalto-Setälä, P. Kallio, Pneumatic cell stretching system for cardiac differentiation and culture, Med. Eng. Phys. 36 (4) (2014) 496–501, https://doi.org/10.1016/j.medengphy.2013.09.008.

[22] P. Roriz, L. Carvalho, O. Frazão, J.L. Santos, J.A. Simões, From conventional sensors to fibre optic sensors for strain and force measurements in biomechanics applications: a review, J. Biomech. 47 (6) (2014) 1251–1261, https://doi.org/10.1016/j.jbiomech.2014.01.054.

[23] A. Velarte, A. Otin, P. Giménez-Gómez, X. Muñoz-Berbel, E. Pueyo, Fiber-optic-based system for high-resolution monitoring of stretch in excised tissues, Biosensors 13 (10) (2023) 900, https://doi.org/10.3390/bios13100900.

[24] A. Sannino, A. Velarte, A. Otín, J.I. Artigas, A. Oliván-Viguera, A flexible PDMS-based optical biosensor for stretch monitoring in cardiac tissue samples, Sensors 23 (23) (2023) 9454, https://doi.org/10.3390/s23239454.

[25] A.M. Salman, A. Al-Janabi, Z.M. Salman, K.M. Salman, S.S. Al-Lami, Zero and double-knotted droplet-shaped optical fiber sensor for rapid temperature variation monitoring, Opt. Contin. 3 (12) (2024) 2360–2368.

[26] S.S. Al-Lami, A.M. Salman, A. Al-Janabi, Wearable macro-bend optical fiber sensor for biomechanical motion evaluation, Opt. Fiber Technol. 81 (2023) 103560.

[27] A. Oliván-Viguera, M. Pérez-Zabalza, L. García-Mendívil, K.A. Mountris, S. Orós-Rodrigo, E. Ramos-Marques, J.M. Vallejo-Gil, P.C. Fresneda-Roldán, J. Fañanás-Mastral, M. Vázquez-Sancho, et al., Minimally invasive system to reliably characterize ventricular electrophysiology from living donors, Sci. Rep. 10 (1) (2020) 19941.

[28] I.D. Johnston, D.K. McCluskey, C.K.L. Tan, M.C. Tracey, Mechanical characterization of bulk Sylgard 184 for microfluidics and microengineering, J. Micromech. Microeng. (2014).

[29] J.N. Lee, C. Park, G.M. Whitesides, Solvent compatibility of poly(dimethylsiloxane)-based microfluidic devices, Anal. Chem. 75 (23) (2003) 6544–6554, https://doi.org/10.1021/ac0346712.

[30] S.S. Al-Lami, H.K. Atea, A.M. Salman, A. Al-Janabi, Adjustable optical fiber displacement-curvature sensor based on macro-bending losses with a coding of optical signal intensity, Sens. Actuators A, Phys. 373 (2024) 115403.

[31] E. Hecht, Optics, Pearson Education, Incorporated, 2017.

[32] V. Prajzler, P. Nekvindova, J. Spirkova, M. Novotny, The evaluation of the refractive indices of bulk and thick polydimethylsiloxane and polydimethyl-diphenylsiloxane elastomers by the prism coupling technique, J. Mater. Sci., Mater. Electron. 28 (11) (2017) 7951–7961.

[33] Y. Xiang, X. Chen, J. Vlassak, Plane-strain bulge test for thin films, J. Mater. Res. 20 (9) (2005) 2360–2370, https://doi.org/10.1557/jmr.2005.0313.

[34] K. Pakazad, Stretchable micro-electrode arrays for electrophysiology, Ph.D. thesis, Delft University of Technology, available at: https://doi.org/10.4233/uuid:d19f10b0-09ef-4009-a337-fbd8a6c20019, 2015.

[35] S. Dogru, B. Aksoy, H. Bayraktar, B.E. Alaca, Poisson's ratio of pdms thin films, Polym. Test. 69 (2018) 375–384.

[36] R. Moučka, M. Sedlačík, J. Osička, V. Pata, Mechanical properties of bulk Sylgard 184 and its extension with silicone oil, Sci. Rep. 11 (1) (2021) 19090, https://doi.org/10.1038/s41598-021-98694-2.

[37] S. Khoshfetrat Pakazad, A. Savov, A. Van De Stolpe, R. Dekker, A novel stretchable micro-electrode array (SMEA) design for directional stretching of cells, J. Micromech. Microeng. 24 (3) (2014) 034003, https://doi.org/10.1088/0960-1317/24/3/034003.

[38] J. Rysä, H. Tokola, H. Ruskoaho, Mechanical stretch induced transcriptomic profiles in cardiac myocytes, Sci. Rep. 8 (1) (2018) 4733, https://doi.org/10.1038/s41598-018-23042-w.

[39] D. Massai, G. Pisani, G. Isu, A. Rodriguez Ruiz, G. Cerino, R. Galluzzi, A. Pisanu, A. Tonoli, C. Bignardi, A.L. Audenino, A. Marsano, U. Morbiducci, Bioreactor platform for biomimetic culture and in situ monitoring of the mechanical response of in vitro engineered models of cardiac tissue, Front. Bioeng. Biotechnol. 8 (2020) 733, https://doi.org/10.3389/fbioe.2020.00733.

[40] D. Ren, J. Song, R. Liu, X. Zeng, X. Yan, Q. Zhang, X. Yuan, Molecular and biomechanical adaptations to mechanical stretch in cultured myotubes, Front. Physiol. 12 (2021) 689492, https://doi.org/10.3389/fphys.2021.689492.

[41] C.A. Dessalles, C. Leclech, A. Castagnino, A.I. Barakat, Integration of substrate- and flow-derived stresses in endothelial cell mechanobiology, Commun. Biol. 4 (1) (2021) 764, https://doi.org/10.1038/s42003-021-02285-w.

[42] Y. Han, J. Yan, Z.-Y. Li, Y.-J. Fan, Z.-L. Jiang, J.Y.-J. Shyy, S. Chien, Cyclic stretch promotes vascular homing of endothelial progenitor cells via Acsl1 regulation of mitochondrial fatty acid oxidation, Proc. Natl. Acad. Sci. USA 120 (6) (2023) e2219630120, https://doi.org/10.1073/pnas.2219630120.

[43] F. Xu, H. Jin, L. Liu, Y. Yang, J. Cen, Y. Wu, S. Chen, D. Sun, Architecture design and advanced manufacturing of heart-on-a-chip: scaffolds, stimulation and sensors, Microsyst. Nanoeng. 10 (1) (2024) 96.